A Flexible, General-Purpose Code Based on the Iterative Physical Optics Algorithm

Analyzing Electromagnetic Scattering in Electrically Large Scenarios. [EM Programmer's Notebook]

Pandolfo, Luca; De Vita, Paolo; Bandinelli, Mauro; Carluccio, Giorgio; Albani, Matteo

DOI
10.1109/MAP.2017.2731210

Publication date
2017

Document Version
Final published version

Published in
IEEE Antennas and Propagation Magazine

David B. Davidson

A Flexible, General-Purpose Code Based on the Iterative Physical Optics Algorithm

Analyzing electromagnetic scattering in electrically large scenarios.

Luca Pandolfo, Paolo De Vita, Mauro Bandinelli, Giorgio Carluccio, and Matteo Albani

A very flexible and efficient iterative physical optics (IPO) algorithm is presented for analyzing the electromagnetic (EM) scattering of complex and electrically large problems. The algorithm accounts for multiple interactions between the objects comprised in the scenarios under the physical optics (PO) approximation. Various techniques for accelerating and parallelizing the algorithm were used, thus obtaining an efficient tool that can be used in novel high-frequency solvers.

EDITOR'S NOTE

Physical optics (PO) remains a powerful tool for solving electromagnetically large problems. This issue's "EM Programmer's Notebook" column describes a PO code based on the iterative PO algorithm. In this article, the theory is briefly reviewed, and a discussion of some aspects of the computational implementation of the method is included. This is followed by several examples of the application of the code to a variety of problems, including reflector antennas, radomes, radar cross section prediction, and antenna siting.

AN ALGORITHM FOR ANALYZING ELECTRICALLY LARGE STRUCTURES

IPO is an iterative high-frequency technique that was originally developed for analyzing the scattering from open-ended cavities with perfectly electrically conducting (PEC) walls [1], [2]. In particular, it was developed to analyze arbitrarily shaped cavities for which analytical waveguide modal methods [3] are not applicable. Indeed, analytical expressions for waveguide modes can only be found for a relatively small set of canonical geometries. Applied to the analyses of waveguides and cavities, IPO allows for better accuracy than ray-based methods such as the shooting and bouncing ray (SBR) method [3], [4] and the generalized ray expansion (GRE) method [5]. Subsequently, it was extended to the case of impedance boundary conditions [6]–[8] and of dielectric thin slabs [9]. More recently it was applied to compute the scattered field and the radar cross section (RCS) of electrically large and realistic complex targets [10], [11], such as tanks and airplanes.

In its various formulations and applications, the authors of the present literature made strong efforts to reduce the computational burden and to accelerate the convergence of the IPO algorithm, especially when dealing with electrically large problems. Concerning the application of IPO to waveguide problems, a first accelerating strategy was adopted in [2] and [7]. Here, the authors resorted to an efficient integration strategy, which consists of integrating the currents progressively, according to the propagation process inside the waveguide, so that each element radiates only over those that follow, first forward and later backward. This technique was called *progressive physical optics* (*PPO*) or *forward–backward IPO*. In [12], the authors proposed a method based on a segmentation of the waveguide/cavity. For each segment of the waveguide, a standard IPO or PPO technique is used. The interactions between the various segments are performed by recurring to scattering matrixes. This approach is particularly suitable when dealing with deep waveguides. Techniques based on the domain decomposition of the scatterer surface were introduced in [7], [13], and [14]. In [7] and [13], the fast far-field approximation

Digital Object Identifier 10.1109/MAP.2017.2731210
Date of publication: 4 October 2017

(FaFFA) algorithm [15] was adopted for accelerating the computational burden relevant to the interactions between the various elements in the scenario under analysis at each iteration. Furthermore, in [7] and [13], iterative relaxation techniques, such as the Jacobi minimal residual (JMRES), were used to control the convergence of the IPO algorithm. In [16]–[18], the authors discuss the possibility of parallelizing and accelerating the computational burden of the IPO algorithm by using graphics processing units (GPUs).

The PO formulation of the IPO algorithm we present allows for the treatment of PEC structures as well as impedance boundary structures and multilayered electrically thin slabs. Furthermore, we discuss various techniques used in its implementation that allow its efficient computational parallelization and acceleration. Thus, the developed algorithm constitutes a powerful tool for analyzing electrically large structures. It is highly versatile in analyzing different EM scenarios that full-wave techniques cannot analyze (large scenarios in terms of the wavelength), and it does not present the typical problems of ray techniques, such as shadow boundary discontinuities and field singularities at caustics. Note that an $e^{j\omega t}$ time dependence for the field is assumed and suppressed throughout this article.

IPO ALGORITHM

EM FORMULATION

The IPO algorithm is based on the application of the equivalence theorem for the description of the scattering of a complex scenario. The equivalent currents are estimated by using the PO approximation for both impenetrable (PEC or impedance boundary condition) and penetrable (thin dielectric slabs) objects. The iterative process permits the reconstruction of the interactions between the objects without resorting to ray tracing. The algorithm reconstructs the reflections from the objects and the forward scattering, which produces a shadow behind an object, and also the masking of the incident field on another object or portion thereof located behind the first. At each iteration, a further reflection (or masking) step is introduced to the description of scattering. The estimate of equivalent currents is therefore similar to that produced by a tracking algorithm in geometrical optics (GO) rays up to an order of interaction equal to the number of steps in the IPO algorithm. On the other hand, the IPO algorithm avoids the ray-tracing operation, which is replaced by the calculation of the scattered field from the surfaces at each iteration. In addition, the IPO algorithm, compared to the multiple-reflection GO ray-based algorithm, also introduces diffractive contributions (under PO approximation) that, although not asymptotically correct, avoid the sharp boundaries present in the estimate of GO ray-based current.

The algorithm is structured as follows. First, we introduce two different kind of scattering object basic blocks: the surface and the plate. The *surface* refers to any surface, or a portion of a surface, which bounds an impenetrable volumetric scatterer. A unit normal vector $\hat{\mathbf{n}}$ pointing outward from the scatterer is associated with each surface object. The term *plate* refers to a panel whose thickness is electrically small, i.e., small in terms of the wavelength. A plate can be considered the union of two surfaces with the opposite unit normal vector. Consequently, the choice of a normal reference for a plate is arbitrary. The introduction of these two kinds of objects is useful for the definition of the updating rules in the iterative algorithm.

According to the IPO algorithm, at the first step, the electric $(\mathbf{J})$ and magnetic $(\mathbf{M})$ currents induced on a point Q of a surface can be calculated as

$$\mathbf{J}^{(0)}(Q) = \begin{cases} \hat{\mathbf{n}} \times (\underline{\mathbf{1}} + \underline{\mathbf{R}}_h) \cdot \mathbf{H}^i(Q) & : \hat{\mathbf{n}} \cdot \hat{\mathbf{k}}^i < 0 \\ 0 & : \hat{\mathbf{n}} \cdot \hat{\mathbf{k}}^i \geq 0 \end{cases} \tag{1}$$

and

$$\mathbf{M}^{(0)}(Q) = \begin{cases} -\hat{\mathbf{n}} \times (\underline{\mathbf{1}} + \underline{\mathbf{R}}_e) \cdot \mathbf{E}^i(Q) & : \hat{\mathbf{n}} \cdot \hat{\mathbf{k}}^i < 0 \\ 0 & : \hat{\mathbf{n}} \cdot \hat{\mathbf{k}}^i \geq 0' \end{cases} \tag{2}$$

respectively, where $\mathbf{E}^i(Q)$ and $\mathbf{H}^i(Q)$ are the electric and magnetic fields illuminating the point Q when all the other objects considered in the scenario are not present; $\underline{\mathbf{R}}_e$ and $\underline{\mathbf{R}}_h$ are the dyadic reflection coefficients at Q for the electric and magnetic fields, respectively; $\underline{\mathbf{1}}$ is the unit dyad; and $\hat{\mathbf{k}}^i$ is the unit propagation vector of the local incident plane wave associated to the incident electric and magnetic field $(\mathbf{E}^i, \mathbf{H}^i)$. Conversely, with $\hat{\mathbf{n}}$ being the normal reference for a plate, the first step currents can be calculated as

$$\mathbf{J}^{(0)}(Q) = \pm\, \hat{\mathbf{n}} \times (\underline{\mathbf{1}} + \underline{\mathbf{R}}_h^{\pm} - \underline{\mathbf{T}}_h^{\pm}) \cdot \mathbf{H}^i(Q) : \hat{\mathbf{n}} \cdot \hat{\mathbf{k}}^i \lessgtr 0 \tag{3}$$

and

$$\mathbf{M}^{(0)}(Q) = \pm\, (\underline{\mathbf{1}} + \underline{\mathbf{R}}_e^{\pm} - \underline{\mathbf{T}}_e^{\pm}) \cdot \mathbf{E}^i(Q) \times \hat{\mathbf{n}} : \hat{\mathbf{n}} \cdot \hat{\mathbf{k}}^i \lessgtr 0, \tag{4}$$

where $\underline{\mathbf{T}}_e$ and $\underline{\mathbf{T}}_h$ are the dyadic transmission coefficients at Q for the electric and magnetic fields, respectively. In writing (3) and (4), we assumed that the thickness of the scattering panel is negligible and the two surfaces constituting the plate overlap. The superscript $\pm$ at the reflection and transmission coefficients takes into account that, depending on which side the plate is illuminated, they have in general a different value.

The IPO iterative updating rule states that, at the iteration q, the IPO currents can be estimated as

$$\mathbf{J}^{(q)}(Q) = \mathbf{J}^{(0)}(Q) + \hat{\mathbf{n}} \times \mathbf{H}_{IPO}[\mathbf{J}^{(q-1)}] + \hat{\mathbf{n}} \times \mathbf{H}_{IPO}[\mathbf{M}^{(q-1)}] \tag{5}$$

and

$$\mathbf{M}^{(q)}(Q) = \mathbf{M}^{(0)}(Q) + \mathbf{E}_{IPO}[\mathbf{J}^{(q-1)}] \times \hat{\mathbf{n}} + \mathbf{E}_{IPO}[\mathbf{M}^{(q-1)}] \times \hat{\mathbf{n}}, \tag{6}$$

where $\mathbf{E}_{IPO}[\mathbf{J}^{(q-1)}]$ and $\mathbf{H}_{IPO}[\mathbf{J}^{(q-1)}]$ are the electric and magnetic fields at Q induced by the electric currents (of the $q-1$th iteration) flowing on the other objects comprised in the entire scenario, whereas $\mathbf{E}_{IPO}[\mathbf{M}^{(q-1)}]$ and $\mathbf{H}_{IPO}[\mathbf{M}^{(q-1)}]$ are the electric and magnetic fields at Q induced by the magnetic currents of the $q-1$th iteration.

The explicit expressions for the electric $\mathbf{E}_{IPO}$ and magnetic $\mathbf{H}_{IPO}$ field involved in (5) and (6) are

$$
\begin{aligned}
&\mathbf{H}_{IPO}[\mathbf{J}^{(q-1)}] \\
&= \sum_{n}^{N} A_n[\underline{\mathbf{1}} + \underline{\mathbf{R}}_h] \cdot [\mathbf{J}^{(q-1)}(\mathbf{r}'_n) \times \hat{\mathbf{R}}_{mn}] \\
&\quad \cdot \frac{e^{-jkR_{mn}}}{4\pi R_{mn}}\left(jk + \frac{1}{R_{mn}}\right)\Bigg|_{\substack{m \neq n \\ \hat{\mathbf{n}}(\mathbf{r}_m)\cdot\hat{\mathbf{R}}_{mn} < 0}} \\
&\mathbf{H}_{IPO}[\mathbf{M}^{(q-1)}] \\
&= -j\omega\varepsilon_0 \sum_{n}^{N} A_n[\underline{\mathbf{1}} + \underline{\mathbf{R}}_h] . \left(\underline{\mathbf{1}} + \frac{\nabla\nabla}{k^2}\right) \\
&\quad \cdot \frac{e^{-jkR_{mn}}}{4\pi R_{mn}} \cdot \mathbf{M}^{(q-1)}(\mathbf{r}'_n)\Bigg|_{\substack{m \neq n \\ \hat{\mathbf{n}}(\mathbf{r}_m)\cdot\hat{\mathbf{R}}_{mn} < 0}} \\
&\mathbf{E}_{IPO}[\mathbf{J}^{(q-1)}] \\
&= -j\omega\mu_0 \sum_{n}^{N} A_n[\underline{\mathbf{1}} + \underline{\mathbf{R}}_e] . \left(\underline{\mathbf{1}} + \frac{\nabla\nabla}{k^2}\right) \\
&\quad \cdot \frac{e^{-jkR_{mn}}}{4\pi R_{mn}} \cdot \mathbf{J}^{(q-1)}(\mathbf{r}'_n)\Bigg|_{\substack{m \neq n \\ \hat{\mathbf{n}}(\mathbf{r}_m)\cdot\hat{\mathbf{R}}_{mn} < 0}} \\
&\mathbf{E}_{IPO}[\mathbf{M}^{(q-1)}] \\
&= -\sum_{n}^{N} A_n[\underline{\mathbf{1}} + \underline{\mathbf{R}}_e] \cdot [\mathbf{M}^{(q-1)}(\mathbf{r}'_n) \times \hat{\mathbf{R}}_{mn}] \\
&\quad \cdot \frac{e^{-jkR_{mn}}}{4\pi R_{mn}}\left(jk + \frac{1}{R_{mn}}\right)\Bigg|_{\substack{m \neq n \\ \hat{\mathbf{n}}(\mathbf{r}_m)\cdot\hat{\mathbf{R}}_{mn} < 0}}
\end{aligned} \tag{7}
$$

for surfaces and

$$
\begin{aligned}
&\mathbf{H}_{IPO}[\mathbf{J}^{(q-1)}] \\
&= \sum_{n}^{N} (\pm A_n)[\underline{\mathbf{1}} + \underline{\mathbf{R}}_h^{\pm} - \underline{\mathbf{T}}_h^{\pm}] \\
&\quad \cdot [\mathbf{J}^{(q-1)}(\mathbf{r}'_n) \times \hat{\mathbf{R}}_{mn}] \\
&\quad \cdot \frac{e^{-jkR_{mn}}}{4\pi R_{mn}}\left(jk + \frac{1}{R_{mn}}\right)\Bigg|_{\substack{m \neq n \\ \hat{\mathbf{n}}(\mathbf{r}_m)\cdot\hat{\mathbf{R}}_{mn} \lessgtr \mathbf{0}}} \\
&\mathbf{H}_{IPO}[\mathbf{M}^{(q-1)}] \\
&= -j\omega\varepsilon_0 \sum_{n}^{N} (\pm A_n)[\underline{\mathbf{1}} + \underline{\mathbf{R}}_h^{\pm} - \underline{\mathbf{T}}_h^{\pm}] \\
&\quad \cdot \left(\underline{\mathbf{1}} + \frac{\nabla\nabla}{k^2}\right)\frac{e^{-jkR_{mn}}}{4\pi R_{mn}} \cdot \mathbf{M}^{(q-1)}(\mathbf{r}'_n)\Bigg|_{\substack{m \neq n \\ \hat{\mathbf{n}}(\mathbf{r}_m)\cdot\hat{\mathbf{R}}_{mn} \lessgtr 0}} \\
&\mathbf{E}_{IPO}[\mathbf{J}^{(q-1)}] \\
&= -j\omega\mu_0 \sum_{n}^{N} (\pm A_n)[\underline{\mathbf{1}} + \underline{\mathbf{R}}_e^{\pm} - \underline{\mathbf{T}}_e^{\pm}] \\
&\quad \cdot \left(\underline{\mathbf{1}} + \frac{\nabla\nabla}{k^2}\right)\frac{e^{-jkR_{mn}}}{4\pi R_{mn}} \cdot \mathbf{J}^{(q-1)}(\mathbf{r}'_n)\Bigg|_{\substack{m \neq n \\ \hat{\mathbf{n}}(\mathbf{r}_m)\cdot\hat{\mathbf{R}}_{mn} \lessgtr 0}} \\
&\mathbf{E}_{IPO}[\mathbf{M}^{(q-1)}] \\
&= -\sum_{n}^{N} (\pm A_n)[\underline{\mathbf{1}} + \underline{\mathbf{R}}_e^{\pm} - \underline{\mathbf{T}}_e^{\pm}] \\
&\quad \cdot [\mathbf{M}^{(q-1)}(\mathbf{r}'_n) \times \hat{\mathbf{R}}_{mn}] \\
&\quad \cdot \frac{e^{-jkR_{mn}}}{4\pi R_{mn}}\left(jk + \frac{1}{R_{mn}}\right)\Bigg|_{\substack{m \neq n \\ \hat{\mathbf{n}}(\mathbf{r}_m)\cdot\hat{\mathbf{R}}_{mn} \lessgtr 0}}
\end{aligned} \tag{8}
$$

for plates. In (7) and (8), $\mathbf{r}'_n$ identifies the position of the nth radiating element; $\mathbf{R}_{mn} = \mathbf{r}_m - \mathbf{r}'_n$ is the vector joining the position of the nth radiating element and the position $\mathbf{r}_m$ of the mth observation point ($\hat{\mathbf{R}}_{mn}$ is the relevant unit vector whereas R_{mn} is the relevant length); A_n is the area of the nth facet, by which the objects are discretized; and ε_0 and μ_0 are the free-space electric permittivity and magnetic permeability, respectively.

FaFFA ALGORITHM

When the scenario to be analyzed is electrically very large, the IPO algorithm complexity becomes too high to maintain an acceptable run time. In such a case, the FaFFA algorithm [7], [13], [15] can be conveniently used to accelerate the calculation of the induced currents at each step of the iterative procedure as well as the PO currents produced by the source and the scattered field.

The FaFFA algorithm is based on a domain decomposition of the scenario under analysis. The currents are grouped into blocks. The interaction between currents belonging to the same block or to near-field block pairs (i.e., different blocks but closer than their far-field distance $2D^2/\lambda$) is evaluated directly (see Figure 1).

The interaction of currents belonging to far-field block pairs is performed in a three-step scheme. First, the field contributions of all currents in the source block are computed at the center of the block (aggregation) and then translated on the center of the observation block (translation). Finally, the contributions for all test currents in the observation block are evaluated by applying a location-dependent phase shift on the center field (disaggregation). Such a procedure reduces the complexity of the algorithm for the calculation of the interaction between two blocks from quadratic to linear; i.e., from $O(M^2)$ to $O(M)$, with M being the average number of elements per block. It can be demonstrated that, with an optimally chosen number of currents per block $M \approx N^{1/2}$, the overall computational complexity of the algorithm is $O(N^{1.5})$, with N denoting the number of elements.

The far-field distance, assumed as $2D^2/\lambda$, might be reduced or increased to trade off between calculation accuracy and speed. Set a required accuracy and the corresponding far-field distance, the FaFFA performance, still depends on the dimension D of the decomposition blocks; therefore, to obtain the best performance, an automatic rule has been implemented to find the optimal blocks dimension.

A further reduction of the complexity can be obtained by exploiting an interpolation according to the multilevel fast multipole algorithm (MLFMA), as described in [15], thus reaching the complexity order $O(N^{1.33})$.

OpenMP AND MULTI-GPU PARALLEL IMPLEMENTATION

The code was parallelized by using OpenMP directives. The standard version of the code assigns the calculation of the current at different test elements to different threads; on the other hand, the code version accelerated by the FaFFA technique assigns different observation blocks to different threads so that the domain decomposition of the structure is performed consistently to the FaFFA scheme. A similar parallelization was also applied to the computation of the PO currents produced by the primary source and to the calculation of the field at the observation points.

In addition to the OpenMP parallelization, the GPU acceleration of the IPO algorithm has also been implemented since it requires significant computational

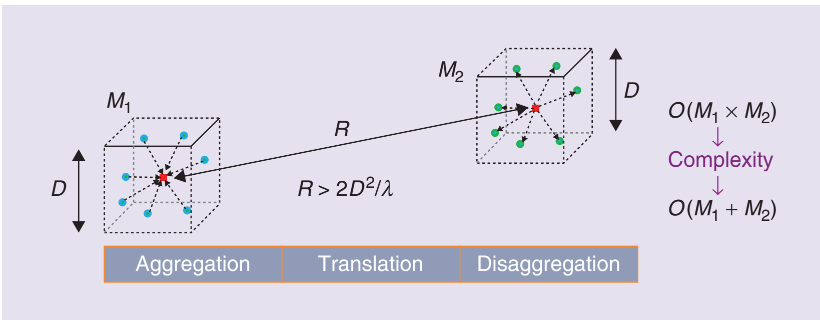

FIGURE 1. A far-field box interaction in FaFFA acceleration.

work and little memory occupancy. Thus, it is well suited for application on a GPU. To this end, the compute unified device architecture (CUDA) by NVIDIA has been used to develop a GPU implementation of the algorithm.

The double precision support offered by the Tesla architecture is used to provide a high level of accuracy. The single GPU CUDA implementation of the algorithm is able to attain a speed increase of 20 times over the central processing unit (CPU) OpenMP parallel execution, while the multi-GPU architecture promises further acceleration (equal to the number of GPU used) and the ability to run very large scenarios on a GPU cluster.

ITERATIVE RULES

In the developed IPO code, a standard Jacobi iterative solver and the JMRES introduced in [13] have been implemented. A relaxation factor of 0.7 in the Jacobi method showed the fastest convergence for the analyzed test cases. JMRES provides, in most cases, better convergence behavior than Jacobi; this is in agreement with [13]. To preserve the parallelizability of the code, iterative methods not compatible with a parallelization scheme such as the Gauss–Seidel were not considered.

Capabilities of monitoring the residual error over the structure for each iterative step have been investigated. In detail, the convergence of the algorithm can be monitored by using various either global or local parameters. A suitable global parameter is

$$\varepsilon_{\mathbf{K}}^{(q)} = \frac{\sqrt{\int_S |\Delta \mathbf{K}^{(q)}|^2 dS}}{\sqrt{\int_S |\mathbf{K}^{(0)}|^2 dS}},$$
$$\Delta \mathbf{K}^{(q)} = \mathbf{K}^{(q)} - \mathbf{K}^{(q-1)}, \tag{9}$$

where $\mathbf{K} = \mathbf{J}, \mathbf{M}$, which gives an estimation of the variation of the electric and magnetic currents at each iteration. The possibility of stopping and resuming the algorithm at each iteration has also been integrated.

APPLICATION OF THE IPO ALGORITHM TO THE EM ANALYSIS OF VARIOUS SCENARIOS

Some examples of the developed IPO code, which is integrated in the Ingegneria Dei Sistemi EM computer-aided engineering tools palette, are reported having in mind two different scopes. The first one is to validate the developed IPO algorithm against simple canonical (or not electrically large) structures, for which reference results coming from full-wave simulators or measurements are available. The second one is to demonstrate IPO applicability with respect to different kinds of problems of interest for the EM community. This issue is addressed by also investigating application fields different than those for which IPO has been originally proposed. Advantages and limitations of the method are therefore discussed to frame IPO in the scenario of computational EM for antennas and platforms.

VALIDATION BY A CANONICAL STRUCTURE: THE SCATTERING OF A TRIHEDRON

We present two simple examples that prove the effectiveness of the discussed algorithm, bearing in mind the goal of validating the developed IPO. In particular, we analyze the scattering of a square trihedron formed by three square plates, intersecting at the origin of the global reference system, whose sides measure 10λ; λ is the free-space (F-S) wavelength.

The structure is illuminated by a z-oriented Hertzian electric dipole with unitary strength located at $P' \equiv (25\lambda, 25\lambda, 25\lambda)$. Figures 2 and 3 report the amplitudes of the scattered electric field estimated on a circular

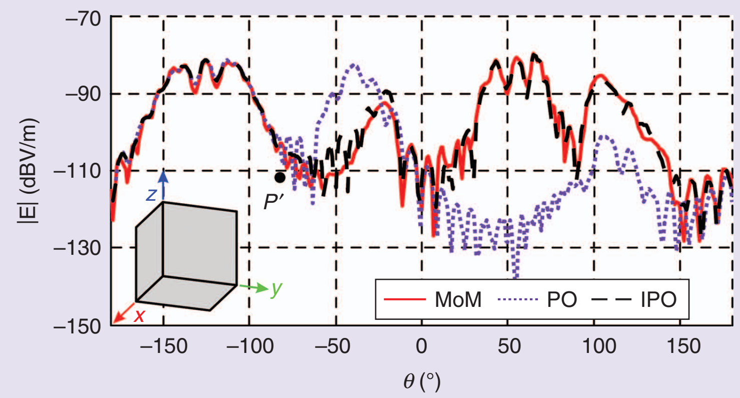

FIGURE 2. The amplitude of the electric field scattered by the PEC trihedron. The reference geometry is shown in the inset. MoM: method of moments.

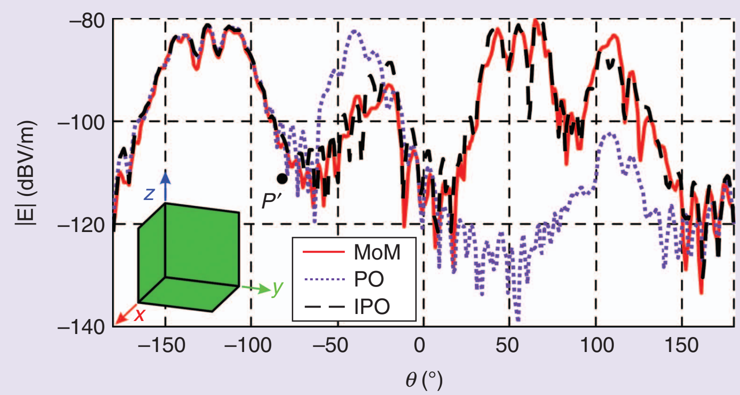

FIGURE 3. The amplitude of the electric field scattered by the dielectric trihedron. The reference geometry is shown in the inset.

scan with a radius of 100λ in the $\phi = 45^\circ$ plane. In the first example, we consider a PEC trihedron (Figure 2), whereas in the second example the trihedron is formed by three dielectric slabs with the dielectric constant $\varepsilon_r = 12$ and a thickness of 0.1λ. In both the examples, we compare the results obtained by the IPO algorithm (black dashed line) against the PO solution (blue dotted line) and the reference method of moments (MoM) solution (red solid line). Figures 2 and 3 show that the IPO solution is in fair agreement with the MoM in the angular regions dominated by the GO scattering; i.e., close to $\theta \sim -120^\circ$, where the forward GO shadow radiation is present, and close to $\theta \sim 50^\circ$ and $\theta \sim 110^\circ$, where multiple GO reflections dominate in the scattered field. As expected, the PO solution is able to recover the zero-order interaction shadow radiation, but it is not able to correctly estimate the field in the regions dominated by multiple reflections.

REFLECTOR ANTENNAS

The PO algorithm is usually applied to model reflector antennas, with a sequential multibounce approach in case of multireflectors antennas. While being conceptually simple, such an approach requires user expertise in the selection of the multibounce path. On the contrary, IPO automatically allows the analysis of all possible bouncing paths, stopping the computation based on a convergence threshold while maintaining the same computational complexity. Apart from such a general simplification, IPO is therefore particularly useful in managing those nonstandard configurations in which the interactions among different parts of the antenna are too complex to be preselected by the user.

Concerning large reflector systems, the proposed IPO algorithm was first used to simulate a 30-m near-field Cassegrain antenna up to 10 GHz with a mixed (full-wave/IPO) method approach. The main reflector diameter is $10^3\lambda$ at 10 GHz, which requires a highly efficient parallel implementation of the algorithms. A detailed description of the procedure used in the simulations, along with the main results, can be found in [19].

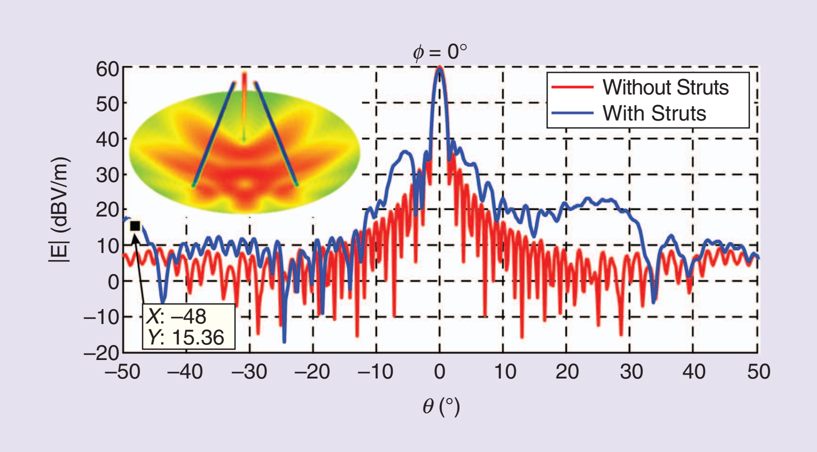

FIGURE 4. A nominal radiation pattern versus a perturbed struts radiation pattern. In the inset, converged current distribution of the IPO four iterations is reported.

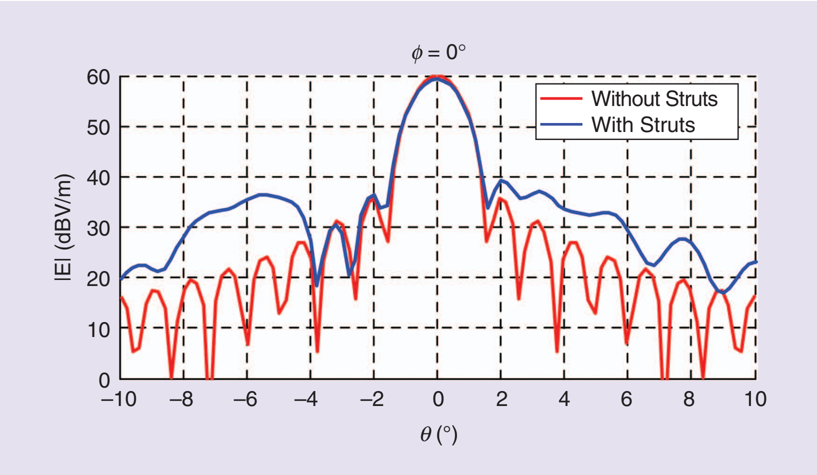

FIGURE 5. A zoomed-in view of the nominal radiation pattern versus the perturbed struts radiation pattern showing the main beam and the near-in sidelobes.

SINGLE REFLECTOR WITH STRUTS

The analysis of a single reflector with a circularly symmetric parabolic surface shape, fed by a horn, is described in the following paragraphs. The feed horn is held in place at the focus by three struts. The example will show the significance of including the scattering from these supports in the analysis. The antenna is designed to operate in the Ka-band at 30 GHz and has the following geometrical characteristics: diameter $D = 500$ mm; focal length $F = 250$ mm; subtended angle from the focal point $\theta = 53.1^\circ$; and strut diameter $d = 100$ mm.

The struts scattering is responsible for two main effects. The feed field is blocked by the struts that create a shadow on the main reflector in the region between the struts and the reflector rim (spherical wave blockage) (see the inset in Figure 4). This effect reduces the aperture efficiency and consequently reduces the peak directivity. Furthermore, the field is scattered onto the antenna, where it will be reflected in a direction away from boresight. This usually gives rise to an increase in the near-in sidelobe level, as we can see in Figure 5 showing a zoom in the near main beam angular region. The struts also block the field reflected from the dish, resulting in a loss of the on-axis directivity (plane wave blockage). The strut scattered field causes a side-lobe increase along the so-called Keller's cone, a cone with an axis along the strut and an opening angle defined by the angle between the strut and the reflector boresight axis. In the present geometry, the main strut scattering direction is 48° with respect to the boresight axis. An increase in the sidelobe level is shown in Figure 4.

COMPACT ANTENNA TEST RANGE WITH SERRATED EDGES

Here the results for a dual parabolic cylindrical reflectors system, employed as a compact test range (CTR), are presented and compared against a full-wave analysis. Detailed IPO and MoM-MLFMA simulation models are developed in Galileo EMT (formerly Antenna Design Framework–ElectroMagnetic Satellite [20]) framework, which allows numerical simulation of compact ranges with arbitrarily shaped serrations and materials.

The system is specifically designed to operate at low frequencies (down to 2 GHz) and at very high frequencies (up to 100 GHz). The compact range reflectors have an electrical size of about $1,200 \times 967\lambda^2$, for a frequency of 100 GHz. These dimensions allow full-wave simulations only in the lower frequency region. Asymptotic methods such as IPO have significantly lower memory requirements and have the advantage of becoming more accurate the larger the structures are.

The Galileo EMT simulation procedure is a simple one-shot procedure in which the complete antenna system, including reflectors and serrations, is modeled by triangular/quadrangular facets. EM-equivalent models are typically input to represent the feeders (typically spherical wave expansion, or electric and magnetic equivalent currents). Parametric Python scripts are also applicable to define geometry, materials, mesh, etc., to facilitate repeated analyses by varying some features of the system. Facilities for monitoring the convergence behavior of IPO are available through different diagnostic parameters: local residual error on each facet of the structure; global residual error (9) over the structure for each iterative step; and structure currents induced on the model as the main output of the iterative procedure (see the inset in Figure 6).

Some results evaluated at 4 GHz using an HP Z800 Workstation Intel Xeon CPU X5672 at 3.20 GHz eight cores with 96 GB of memory are reported for both IPO and MoM-MLFMA algorithms to evaluate IPO accuracy. The near field on the quiet zone (QZ) is evaluated first (Figures 6 and 7). The size of the QZ is 1.8 m × 1.8 m, which corresponds to the range bounded by the square with black lines in Figure 7, where the amplitude of the electric field evaluated by IPO is shown. In Figure 6 the curves relevant to the $y = 0$ m cut are reported both for IPO and MoM-MLFMA.

Pattern comparison along $\phi = 0°$ and $\phi = 90°$ cuts for both IPO and MoM solutions are reported in Figures 8 and 9, respectively. The details of the computational performances are summarized in Table 1. In the proposed example, the IPO algorithm gives results that compare well with the full-wave solution. Moreover, it is easy to use, it significantly reduces the memory requirements, and it is very efficient in computational time, thus allowing CTR accurate analysis at frequencies where full-wave methods require unavailable computational resources.

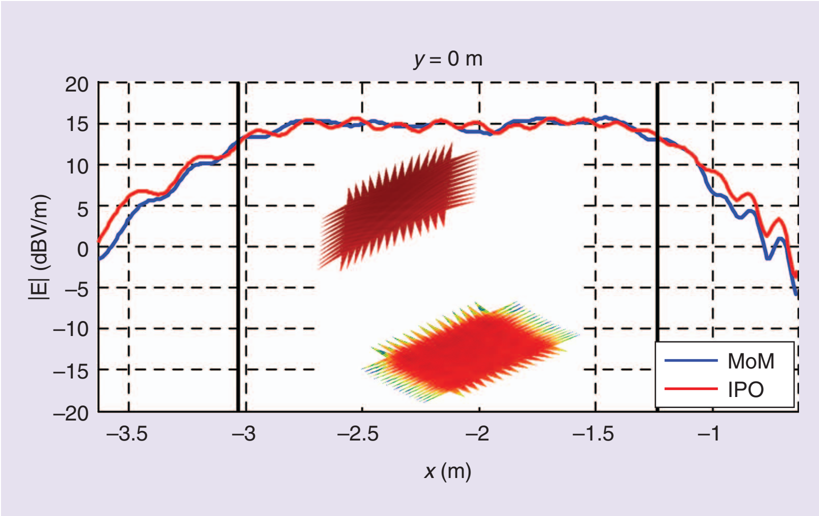

FIGURE 6. The amplitude of the electric field scattered by the CTR on the QZ in the $y = 0$ m cut. The IPO-induced currents at 4 GHz are reported in the inset.

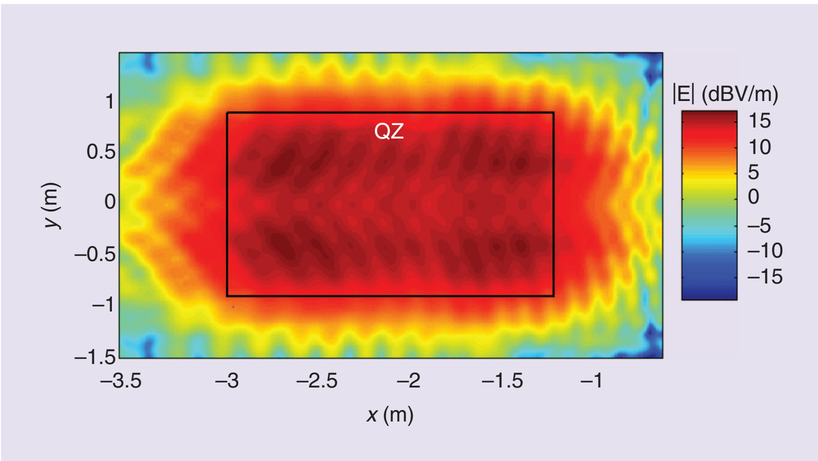

FIGURE 7. The amplitude of the electric field scattered by the CTR in the QZ predicted by the IPO.

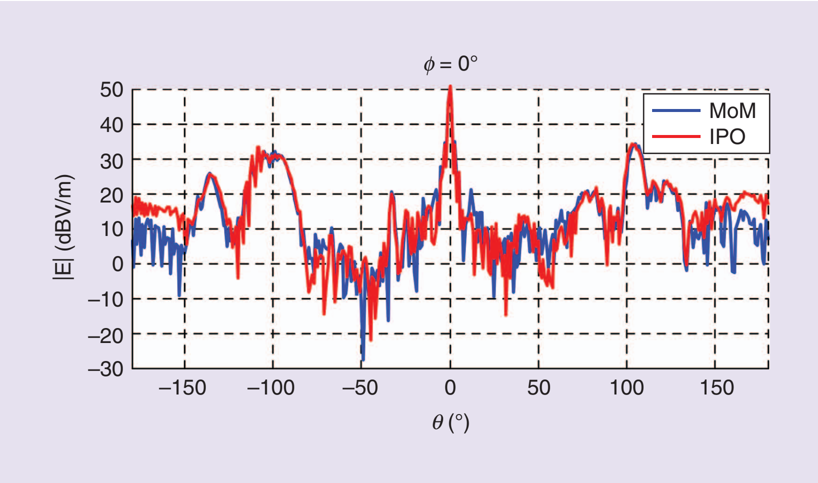

FIGURE 8. The amplitude of the electric far field scattered by the CTR along the $\phi = 0°$ cut.

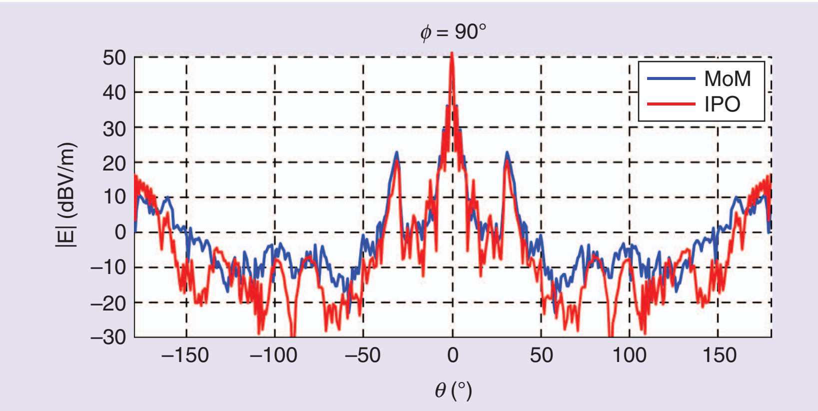

FIGURE 9. The amplitude of the electric far field scattered by the CTR along the $\phi = 90°$ cut.

TABLE 1. THE COMPUTATIONAL PERFORMANCES.

	Facets (*n*)	Threads (*n*)	RAM (GB)	Elapsed Time (min)	Iterations (*n*)
MoM–MLFMA	493,208	8	12 GB	15	30
IPO	89,381	8	0.2 GB	3	3

RADOMES

The assessment of radomes quality requires verification of several antenna performances [21]: transmission efficiency, sidelobe level, incident reflection, beam deflection, and beamwidth. A significant degree of accuracy is required to be able to discriminate between the different classes of quality reported in [21]. However, the large electrical dimension of the radome sometimes limits the applicability of full-wave methods. The implemented IPO algorithm is particularly suitable to such kinds of applications, thanks to its capability to manage partially transparent materials and multibounces while having a much lower computational cost than full-wave methods, thus removing analysis limitations due to the electrical dimensions. In implementing an integral current-based approach, IPO is also much better than ray-based techniques in terms of accuracy.

Here we investigate the impact of an airborne dielectric radome on the radiation pattern of a radar antenna operating in the X band (9.375 GHz). The geometrical model of the radome is obtained as a portion of the A-139 helicopter radome whose computer-aided design model is shown in the inset of Figure 10. The values of permittivity and thickness of the considered monolithic radome are $\varepsilon_r = 3.85$ and $h = 1.58$ mm, respectively. The antenna and its support are depicted in yellow in the inset of Figure 10. The antenna radiates a boresight beam in the helicopter's front direction.

The EM interaction between the antenna and the radome are evaluated by the IPO solver, taking into account multiple reflections and both parallel and perpendicular polarizations. The antenna is modeled as an equivalent current distribution that reproduces the measured radiation patterns, especially in the region corresponding to the main lobe and the first secondary lobes.

The free space radiation pattern of the synthesized antenna has the following features: maximum gain ≈ 28 dB, half-power beamwidth $\approx 8°$, sidelobe level ≈ 25 dB, circular opening (diameter $30\text{ cm} \approx 10\lambda$), and linear polarization.

Radomes can cause high sidelobes in radar-antenna patterns, which will increase clutter, false alarm rate, and susceptibility to jamming. The radomes can also cause deflection and attenuation of the main beam, filling of the difference-pattern null used for tracking, and interferometry errors. The IPO solver can help to predict these effects, providing the following performance parameters: incidence angles on the radome surface, power density on the radome surface, parallel and perpendicular components of the transmission coefficients on the radome, and directivity of the antenna with and without radome (Figure 10).

RCS

The RCS assessment of military platforms in frequency bands used by typical radar threats is a central aspect in the design of a cost-effective electronic warfare defense system. Both naval and avionic targets must be appropriately designed to optimize the dominant scattering phenomena, taking into account the operative environment. For example, the radar signature of a naval vessel is modified by the introduction of the multipath effect due to the sea surface; whereas for an aircraft, it is fundamental to simulate the scattering of the engine air inlet.

The IPO approach is perfectly suitable in this second field of application. In particular, in early-phase design, the IPO solver code can be employed to optimize the engine intake cavity as well as the whole platform, allowing a fast evaluation loop on very large structures in terms of wavelength. Indeed, it is possible to simply evaluate the effect of shape modifications, as well as the use of radar absorbing material to minimize the scattering.

We analyzed the RCS of a Sukhoi aircraft (inset in Figure 11). The HH (copolar horizontal) component of the monostatic RCS of this target was computed by using IPO at 1 GHz for 0–360° azimuth, 0° elevation. The mesh model for IPO consists of 150.974 facets at 1 GHz, corresponding to about 16 facets per square wavelength. The IPO results (Figure 11) compare well with the results obtained by using EM full-wave simulation software implementing an MLFMA.

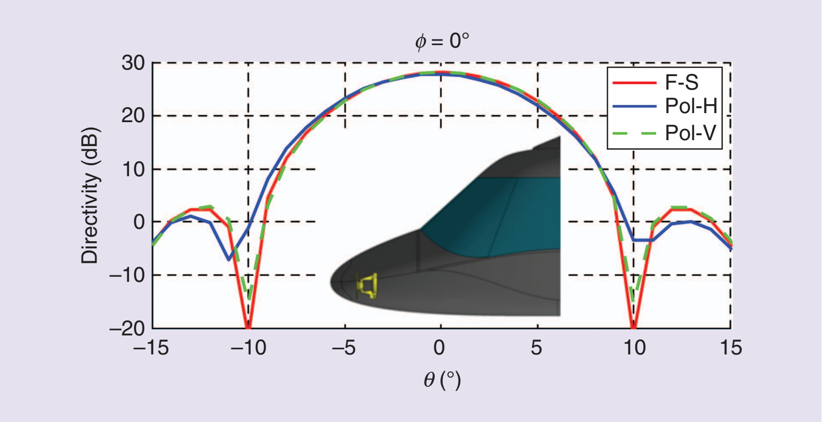

FIGURE 10. The directivity for the different antenna polarizations on the principal cut in the presence of the dielectric radome (blue and green lines). The F-S pattern of the antenna in the absence of radome (red line) is also plotted as a reference. The radome shape and antenna position (in yellow) are reported in the inset. Pol-H: horizontal polarization; Pol-V: vertical polarization.

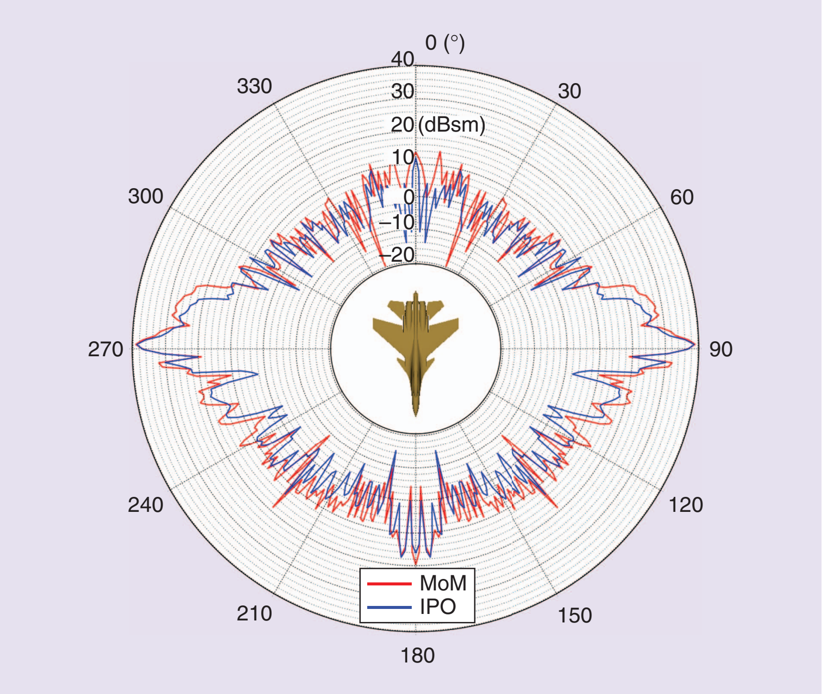

FIGURE 11. The HH-polarized monostatic RCS of a Sukhoi aircraft for 0–360° azimuth and 0° elevation at 1 GHz, showing a comparison between the IPO (blue line) and the MLFMA (red line). The reference geometry is reported in the inset.

ANTENNA SITING

Antenna farms aboard platforms (e.g., ships, aircrafts, and satellites) require the verification of several issues related both to performance (e.g., antenna coverage) and electromagnetic compatibility (e.g., interantenna coupling, near-field hazard, radiated emission/susceptibility). Depending on the antenna working frequency and platform geometrical dimensions, several modeling techniques are usually applied: from full-wave methods in the low-frequency range (e.g., MoM, finite difference time domain) up to ray-based techniques (e.g., uniform theory of diffraction, SBR) in the upper frequency range. As it happens in other application fields, usually an intermediate frequency range exists in which full-wave methods can no longer be applied due to the computational cost exceeding the available computational resources and where ray-based methods suffer from problems of applicability and accuracy. The IPO method can again fill the gap by preserving many of the desirable properties of the full-wave methods, e.g., detailed geometry representation, ease of use, multibouncing, and integral current-based representation.

The problem of the modification of the antenna pattern, due to the antenna interaction with the space-platform on which it has been installed, was studied, i.e., how the spacecraft body, the appendages, and the surrounding antenna systems (considered as passive structures) modify the far-field antenna

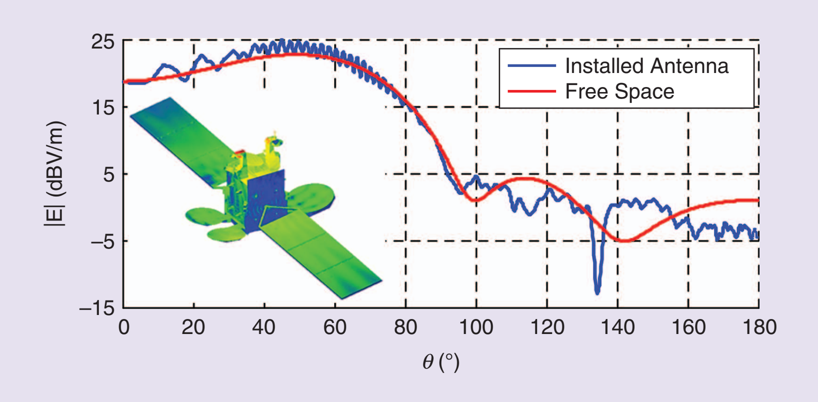

FIGURE 12. The helix antenna nominal F-S radiation pattern (red) and radiation pattern when the antenna is installed on board the satellite (blue). The IPO current distribution on the satellite is shown in the inset.

pattern and, consequently, its projection on Earth. In particular, the pattern distortion of a helix antenna operating at 2 GHz was computed by using IPO. The mesh model consists of 234.165 facets, corresponding to approximately 16 facets per square wavelength. IPO converges in four iterations, providing the currents distribution shown in the inset of Figure 12. In addition, the radiation pattern of the helix antenna in its operating condition is calculated and directly compared against its F-S pattern (Figure 12).

CONCLUDING REMARKS

We have presented a versatile and efficient IPO algorithm. Various techniques for accelerating its computational burden and parallelizing its implementation have been discussed. The effectiveness of the proposed formulation was tested by several numerical examples showing the capabilities and the flexibility of the developed tool in analyzing the EM scattering in different complex, electrically large scenarios. In particular, the tool was validated against reference solutions obtained by different numerical solvers. Further work is in progress to improve the accuracy of the IPO formulation in predicting diffraction effects or currents in shadow regions.

AUTHOR INFORMATION

Luca Pandolfo (l.pandolfo@idscorporation.com) is with the Ingegneria Dei Sistemi S.p.A., Pisa, Italy.

Paolo De Vita (p.devita@idscorporation.com) is with the Ingegneria Dei Sistemi S.p.A., Pisa, Italy.

Mauro Bandinelli (m.bandinelli@idscorporation.com) is with the Ingegneria Dei Sistemi S.p.A., Pisa, Italy.

Giorgio Carluccio (g.carluccio@tudelft.nl) is with the Department of Microelectronics, Delft University of Technology, The Netherlands.

Matteo Albani (matteo.albani@unisi.it) is with the Department of Information Engineering and Mathematics, University of Siena, Italy.

REFERENCES

[1]. F. Obelleiro, J. L. Rodriguez, and R. J. Burkholder, "An iterative physical optics approach for analyzing the electromagnetic scattering by large open-ended cavities," *IEEE Trans. Antennas Propag.*, vol. 43, no. 4, pp. 356–361, Apr. 1995.

[2]. J. L. Rodriguez, F. Obelleiro, and A. G. Pino, "Iterative solutions of MFIE for computing electromagnetic scattering of large open-ended cavities," *IEE Proc. Microw. Antennas Propag.*, vol. 144, no. 2, pp. 141–144, Apr. 1997.

[3]. P. H. Pathak and R. J. Burkholder, "Modal, ray and beam techniques for analyzing the EM scattering by open-ended waveguide cavities," *IEEE Trans. Antennas Propag.*, vol. 37, no. 5, pp. 635–647, May 1989.

[4]. H. Ling, R. C. Chou, and S. W. Lee, "Shooting and bouncing rays: calculating the RCS of an arbitrarily shaped cavity," *IEEE Trans. Antennas Propag.*, vol. 37, no. 2, pp. 194–205, Feb. 1989.

[5]. P. H. Pathak and R. J. Burkholder, "High-frequency electromagnetic scattering by open-ended waveguide cavities," *Radio Sci.*, vol. 26, no. 1, pp. 211–218, Jan.-Feb. 1991.

[6]. F. Obelleiro, M. G. Araújo, and J. L. Rodriguez, "Iterative physical-optics formulation for analyzing large waveguides with lossy walls," *Microwave Opt. Techn. Let.*, vol. 28, no. 1, pp. 21–26, Jan. 2001.

[7]. R. J. Burkholder and T. Lundin, "Forward-backward iterative physical optics algorithm for computing the RCS of open-ended cavities," *IEEE Trans. Antennas Propag.*, vol. 53, no. 2, pp. 793–799, Feb. 2005.

[8]. M. F. Cátedra, C. Delgado, and I. G. Diego, "New physical optics approach for an efficient treatment of multiple bounces in curved bodies defined by an impedance boundary condition," *IEEE Trans. Antennas Propag.*, vol. 56, no. 3, pp. 728–736, Mar. 2008.

[9]. R. Hémon, P. Pouliguen, H. He, J. Saillard, and J. F. Damiens, "Computation of EM field scattered by an open-ended cavity and by a cavity under radome using the iterative physical optics," *Prog. Electromagnetics Res.*, vol. 80, pp. 77–105, 2008.

[10]. R. J. Burkholder, Ç. Tokgöz, C. J. Reddy, and W. O. Coburn, "Iterative physical optics for radar scattering predictions," *Appl. Comput. Electromagnetics Soc. J.*, vol. 24, no. 2, pp. 241–258, Apr. 2009.

[11]. P. Pouliguen, R. Hémon, and J. F. Damiens, "Physical optics for large scale electromagnetic scattering problems," in *Proc. Fourth European Conference Antennas and Propagation (EuCAP)*, Barcelona, Spain, Apr. 2010.

[12]. F. Obelleiro, J. Campos-Niño, J. L. Rodriguez, and A. G. Pino, "A segmented approach for computing the electromagnetic scattering of large and deep cavities," *Prog. Electromagnetics Res.*, vol. 19, pp. 129–145, Jan. 1998.

[13]. R. J. Burkholder, "A fast and rapidly convergent iterative physical optics algorithm for computing the RCS of open-ended cavities," *Appl. Comput. Electromagnetics Soc. J.*, vol. 16, no. 1, pp. 53–60, Mar. 2001.

[14]. A. Boag, "A fast iterative physical optics (FIPO) algorithm based on non-uniform polar grid interpolation," *Microwave Opt. Techn. Let.*, vol. 35, no. 3, pp. 240–244, Nov. 2002.

[15]. C. C. Lu and W. C. Chew, "Fast far-field approximation for calculating the RCS of large objects," *Microwave Opt. Techn. Let.*, vol. 8, no. 5, pp. 238–241, Apr. 1995.

[16]. K. Xu, Z. W. Liu, D. Z. Ding, R. S. Chen, "GPU acceleration of the iterative physical optics (IPO) method," in *Proc. 8th Int. Symposium Antennas, Propagation, and EM Theory*, Kunming, China, Nov. 2008.

[17]. J.-P. Adam, G. Kubické, and R. Hémon, "Iterative physical optics GPU accelerated," in *Proc. 2012 European Conference and Exhibition Electromagnetics (EUROEM)*, Toulouse, July 2012.

[18]. C. Tokgoz and V. Venugopal, "GPU accelerated iterative physical optics to predict RF propagation in urban environments," in *Proc. IEEE Int. Symp. Antennas and Propagation and USNC-URSI National Radio Science Meeting*, Orlando, Florida, July 2013.

[19]. A. D Maria, L. Pandolfo, P. D Vita, G. Guida, M. Bercigli, and M. Bandinelli, "High fidelity modeling of 30 m near-field Cassegrain antenna in X-band," in *Proc. Eight European Conference Antennas and Propagation (EuCAP)*, The Hague, The Netherlands, Apr. 2014.

[20]. M. Sabbadini, G. Guida, and M. Bandinelli, "The antenna design framework—electromagnetic satellite," *IEEE Trans. Antennas Propag.*, vol. 51, no. 2, pp. 225–235, Apr. 2009.

[21]. *RTCA DO-213 Minimum Operational Performance Standards for Nose-Mounted Radomes*, RTCA Standard DO-213, Mar. 17, 2016.